

X-RAY BACKGROUND AT HIGH REDSHIFTS FROM POP III REMNANTS: RESULTS FROM POP III STAR FORMATION RATES IN THE RENAISSANCE SIMULATIONS

HAO XU¹, KYUNGJIN AHN², MICHAEL L. NORMAN¹, JOHN H. WISE³, AND BRIAN W. O'SHEA⁴

¹San Diego Supercomputer Center, University of California, San Diego, 9500 Gilman Drive, La Jolla, CA 92093; hxu@ucsd.edu, mlnorman@ucsd.edu

²Department of Earth Science Education, Chosun University, Gwangju 501-759, Korea; kjahn@chosun.ac.kr

³Center for Relativistic Astrophysics, School of Physics, Georgia Institute of Technology, 837 State Street, Atlanta, GA 30332; jwise@gatech.edu and

⁴Department of Computational Mathematics, Science and Engineering, Department of Physics and Astronomy, and National Superconducting Cyclotron Laboratory, Michigan State University, East Lansing, MI 48824; oshea@msu.edu

Draft version October 10, 2016

ABSTRACT

Due to their long mean free paths, X-rays are expected to have global impacts on the properties of the intergalactic medium (IGM) by their large scale heating and ionizing processes. At high redshifts, X-rays from Population (Pop) III binaries might have important effects on cosmic reionization and the Ly α forest. As a continuation of our previous work on Pop III binary X-rays (Xu et al. 2014), we use the Pop III distribution and evolution from the *Renaissance Simulations*, a suite of self-consistent cosmological radiation hydrodynamics simulations of the formation of the first galaxies, to calculate the X-ray luminosity density and background over the redshift range $20 \geq z \geq 7.6$. As we find that Pop III star formation continues at a low, nearly constant rate to the end of reionization, X-rays are being continuously produced at significant rates compared to other possible X-ray sources, such as AGNs and normal X-ray binaries during the same period of time. We estimate that Pop III binaries produce approximately 6 eV of energy in the X-rays per hydrogen atom. We calculate the X-ray background for different monochromatic photon energies. KeV X-rays redshift and accumulate to produce a strong X-ray background spectrum extending to roughly 500 eV. The X-ray background is strong enough to heat the IGM to ~ 1000 K and to ionize a few percent of the neutral hydrogen. These effects are important for an understanding of the neutral hydrogen hyperfine transition 21-cm line signatures, the Ly α forest, and the Thomson optical depth to the CMB.

Keywords: galaxies: formation – galaxies: high redshift – cosmology—methods:numerical – star formation

1. INTRODUCTION

One of the most important problems in astrophysics and cosmology in both theory and observation is to obtain the thermal and ionization history of the intergalactic medium (IGM) prior, during, and after the epoch of reionization. It is critical to understand cosmological observations, such as high redshift 21-cm neutral hydrogen line signatures, the Thomson scattering optical depth of the CMB, and properties of the Ly α forest.

The appearance of the first luminous objects—likely the first stars—marks the end of the cosmic dark ages after recombination, and the beginning of the last cosmic phase transition of reionization, a prolonged process that ionizes and heats the IGM. The first generation of stars (Population III stars) are believed to have formed from metal-free gas in small dark matter halos and having a large (tens to a few hundreds M_{\odot}) characteristic mass (Abel et al. 2002; Bromm et al. 2002; O'Shea & Norman 2007; Turk et al. 2009; Greif et al. 2012; Hirano et al. 2015; Hosokawa et al. 2016). Pop III stars have short lifetimes (Schaefer 2002) and may explode as supernovae (SNe), enriching their surrounding IGM. Once the gas metallicity passes some critical threshold, $\sim 10^{-6} Z_{\odot}$ if dust cooling is efficient (Omukai et al. 2005; Schneider et al. 2006; Clark et al. 2008) or $\sim 10^{-3.5} Z_{\odot}$ otherwise (Bromm et al. 2001; Smith et al. 2009), the gas can cool efficiently and lower its Jeans mass and form (Pop II) stars in clusters at much higher rates. This makes the Pop III period of a given galaxy short. Consequently it is believed that Pop III stars are not a major contributor to the UV photons responsible for reionization (e.g. Fan et al. 2006). (However see Wise & Abel (2008) and Ahn et al. (2012) for their contribution to the *start* of reion-

ization).

X-ray radiation with its much longer mean free path than UV radiation has been considered a good candidate for the pre-ionization and pre-heating the IGM much earlier than the end of the reionization at $z \sim 6$ (e.g., Oh 2001; Venkatesan et al. 2001; Ricotti & Ostriker 2004; Ricotti et al. 2005), and for smooth heating of the IGM; e.g. (Haiman 2011). Its impact on the high redshift 21cm signal has been explored by many authors (Pritchard & Furlanetto 2007; Mirabel et al. 2011; Pritchard & Loeb 2012; Visbal et al. 2012; Pacucci et al. 2014; Fialkov & Barkana 2014; Mirocha et al. 2016), and observational constraints on the cosmic X-ray background have been investigated by Fialkov et al. (2016). Recent cosmological simulations (Turk et al. 2009; Stacy et al. 2010; Susa et al. 2014) have found that metal-free star-forming clouds might fragment to form binaries in a non-negligible fraction of Pop III star forming events, making Pop III stars and remnants possible strong X-ray sources at high redshifts. Pop III in the approximate mass range $40 - 140 M_{\odot}$ and $> 260 M_{\odot}$ may directly collapse to form black holes (BHs; Heger et al. 2003). Any strong accretion onto these massive Pop III seed BHs would lead to X-ray radiation at high redshifts (Kuhlen & Madau 2005; Alvarez et al. 2009; Tanaka et al. 2012; Visbal et al. 2012). X-rays from Pop III binaries have been suggested to produce a pre-heated IGM (e.g., Mirabel et al. 2011; Haiman 2011; Visbal et al. 2012; Mesinger et al. 2013; Fialkov et al. 2014; Madau & Fragos 2016), and to partially ionize the IGM in large volumes (e.g., Ostriker & Gnedin 1996; Pritchard & Furlanetto 2007). Xu et al. (2014) showed that Pop III binaries might be the dominant X-ray sources at high redshifts and discussed how the IGM might be heated locally

by hundred eV photons and globally by the X-ray background from keV photons. Homogeneously heating of the IGM on tens to hundreds Mpc scales by an X-ray background may be important to understand the linewidths of Ly α forest spectra (Tytler et al. 2009) and high- z 21-cm neutral hydrogen line signatures (Ahn et al. 2015).

Recently, Xu et al. (2016a) showed using numerical simulations that Pop III stars can form continuously at significant rates from redshifts higher than 20 down to the end of the reionization. This suggests that X-rays from Pop III binaries might continue to be important X-ray sources till the end of the reionization and the X-ray background may heat the IGM for a long enough period to significantly heat the IGM globally. In this *Letter*, we estimate the X-ray luminosities from Pop III binaries using the results of the *Renaissance Simulations* (Xu et al. 2013; O’Shea et al. 2015; Xu et al. 2016b) and calculate the X-ray background using simple models. This paper extends to lower redshifts the results first presented in Xu et al. (2014) concerning the X-ray background itself; we defer to a future paper a detailed calculation of the heating and ionization of the IGM and its 21cm signature. We first describe the simulations and X-ray source and background models in Section 2. In Section 3, we present our results for the X-ray luminosity density, and the background intensity and spectra. We discuss the implications of this strong X-ray background from Pop III stars in Section 4.

2. THE RENAISSANCE SIMULATIONS AND X-RAY MODELS

The *Renaissance Simulations* are a suite of adaptive mesh refinement (AMR) first galaxy formation simulations carried out using the ENZO¹ code (Bryan et al. 2014) on the Blue Waters supercomputer operated by NCSA/UTUC. ENZO has been used extensively for high redshift structure formation research (e.g., Abel et al. 2002; O’Shea & Norman 2007; Xu et al. 2008; Turk et al. 2009; Wise et al. 2012a,b; Xu et al. 2013; Wise et al. 2014). Notably, UV ionizing radiation from stellar populations is followed using the MORAY adaptive ray tracing radiation transport solver (Wise & Abel 2011). Lyman-Werner radiation transport from stellar sources is calculated without considering absorption using ray-tracing as well. However, we included the attenuation of LW photons, by a grey opacity approximation, the “picket-fence” modulation factor, as a function of the comoving distance between the source and the observer (Ahn et al. 2009). The baryonic properties are calculated using a 9-species primordial non-equilibrium gas chemistry and cooling network (Abel et al. 1997), supplemented by metal-dependent cooling tables (Smith et al. 2009). Prescriptions for Population III and metal-enriched star formation and feedback are employed which have been fully described in Xu et al. (2013) and Wise et al. (2012b). Here we briefly summarize the Pop III prescriptions because they are the focus of this paper. Individual Pop III star particles are created when the overdensity, cooling time, H_2 fraction, and metallicity thresholds given in Wise et al. (2012a) are obeyed. The stellar mass, which dictates its lifetime and fate is drawn from a top-heavy IMF with a characteristic mass of $40M_\odot$. The UV hydrogen ionizing and LW photon luminosities and lifetimes of the Pop III stars are determined by the mass-dependent model from Schaerer (2002). Depending on their mass, they can end their lives as Type II or pair instability SNe, or collapse directly to black holes (Heger et al. 2003). Kinetic and metal yields for the SNe are taken

from Heger et al. (2003). Pop III stellar remnants’ positions are tracked for the duration of the simulation as they become incorporated into more massive halos. Their population statistics were examined in Xu et al. (2013).

The simulated box is a region of the universe with 28.4 comoving Mpc/h on a side (or 40 Mpc with $h = 0.71$). This is more than adequate to sample the large fluctuations in the space density of Pop III star-forming minihalos (Barkana & Loeb 2004). We do not include the streaming velocity effect which modulates Pop III star formation on yet larger scales (Fialkov et al. 2013) because our Lyman-Werner regulated Pop III star formation occurs in minihalos with $M_h > 5 \times 10^6 M_\odot$ (Xu et al. 2013, 2016a) where the streaming effect is negligible (Stacy et al. 2011; Greif et al. 2011). The simulations use the WMAP7 Λ CDM+SZ+LENS best fit cosmology (Komatsu et al. 2011): $\Omega_M = 0.266$, $\Omega_\Lambda = 0.734$, $\Omega_b = 0.0449$, $h = 0.71$, $\sigma_8 = 0.81$, and $n = 0.963$. Initial conditions were generated at $z = 99$ using MUSIC (Hahn & Abel 2011), and a low-resolution (512^3 root grid) simulation was run to $z = 6$ to find regions suitable for re-simulation. The simulation volume was then smoothed on a physical scale of 6 comoving Mpc, and regions of high ($\langle\delta\rangle \equiv \langle\rho\rangle/(\Omega_M\rho_C) - 1 \simeq 0.68$), average ($\langle\delta\rangle \simeq 0.09$), and low ($\langle\delta\rangle \simeq -0.26$) mean density (at $z = 15, 12.5$, and 8 , respectively) were chosen for re-simulation. These subvolumes, hereafter designated the “Rarepeak,” “Normal,” and “Void” regions, with comoving volumes of 133.6, 220.5, and 220.5 Mpc^3 , were resimulated with three additional static nested grids, resulting in an effective initial resolution of 4096^3 grid cells and particles in the region of interest, translating to a dark matter mass resolution of $2.9 \times 10^4 M_\odot$ in the same region. We allowed further local refinement (and then, the star formation) in the Lagrangian volume of the finest nested grid based on baryon or dark matter overdensity for up to 12 total levels of refinement (i.e., a comoving resolution of 19 pc in the finest cells.) For more details about the calculations and scientific results about *Renaissance Simulations*, see Xu et al. (2013, 2014); Chen et al. (2014); O’Shea et al. (2015).

The X-ray source and background models have been employed in Xu et al. (2014) and Ahn et al. (2015). Here we summarize the basic assumptions and approach. The X-ray source model assumes that a fraction $\epsilon_{\text{bin}} = 0.5$ of Pop III stars form in binaries, and evolve to become high mass X-ray binaries (XRB) which emit X-rays for a fixed lifetime $\tau = 30$ Myr. We use the same luminosities as in Xu et al. (2014) to calculate the X-rays emitted in the AMR-refined volumes. To calculate the X-ray background, we need to estimate the X-ray emission coming from the non-refined regions, in which star formation is not resolved. We do this in two different ways. In Method 1, we adopt the same simple prescription described in Xu et al. (2014); namely for every root grid cell in the refinement volume containing X-ray emitting sources, we sum up their baryon density ρ and X-ray luminosity L . Dividing by the number of emitting cells we have their average values $\bar{\rho}$ and \bar{L} . Then, in the unrefined portion of the simulation volume, if the root grid cell’s baryon density $\rho \geq \bar{\rho}$, we assign it an X-ray luminosity \bar{L} . The defect of this model is that it predicts different amounts of total emission from the unresolved region, which is mostly common to each simulation. This is due to the different mean densities of the refined regions. To deal with this problem we introduce Method 2, in which we combine the results from all three refined regions to predict the X-ray emission at every redshift. For each root grid cell in

¹ <http://enzo-project.org/>

the three survey volumes at each redshift, we record $L \geq 0$, ρ , and a smoothed density over a ~ 1 Mpc sphere ρ_s centered on the cell. From this data we apply machine learning algorithms from the Python toolkit `scikit-learn` to derive two functions: $P_X(\rho, \rho_s, z)$ and $L_X(\rho, \rho_s, z)$. P_X is the normalized probability that a cell with values (ρ, ρ_s, z) contains one or more X-ray sources. We assume the probability can be represented as a second order polynomial in z , ρ and ρ_s and fit it using all data from three simulations at all redshifts. L_X is a second order polynomial fit to the dimensional X-ray luminosity for only those cells with $L > 0$. Armed with these two functions we now walk through the cells in the unrefined region and draw a random number to compare with P_X to decide whether it contains X-ray sources. If it does, we assign it an X-ray luminosity using L_X . In this way, we generate the X-ray emissivity field in the unrefined root grid for all redshift outputs in each of the three simulations. As we will see in the next section, Method 1 provides only a rough estimate, for the reason stated, and is not recommended. Method 2 is more robust because it is based on fitting far more data from different redshifts and environments. It is nonetheless worthwhile presenting both as it provides a quantitative estimate for the error.

Given the X-ray emissivity everywhere in the 40 Mpc periodic volume, we perform the same calculations as in [Xu et al. \(2014\)](#), Sec. 5.2 to estimate the X-ray background. We locate the 3D field of X-ray luminosities frozen at the most recent past in the full box periodically, and calculate the contribution at every location of the box by summing over the full contribution from all the X-ray sources but within the corresponding lookback time. We simply treat the background sources to be uniformly distributed, since inhomogeneity in the source distribution at large lookback times will be observed to be almost uniform inside the box. Here, we assume that the whole simulation box is a good representation of the average universe and take its luminosity as the mean, globally averaged luminosity, and we also consider the absorption of photons by H I and He I with cosmic mean density.

Simulation data were processed and analyzed using YT² ([Turk et al. 2011](#)) on the Blue Waters system at NCSA, the Gordon system at SDSC, and the Wrangler system at TACC.

3. RESULTS

Before we show the results of X-ray generation and background, we illustrate the Pop III star formation rate densities from the three simulated volumes in Figure 1. The Pop III star formation rate density is simply correlated with the mean matter overdensity. The *Rarepeak* simulation has earlier Pop III star formation and higher formation rate. The *Void* region is the only simulation we can run to single digit redshifts. Its Pop III star formation starts late at $z \sim 20$ and the rate density increases to $\sim 10^{-5} \text{ M}_\odot \text{ yr}^{-1} \text{ Mpc}^{-3}$ at $z \sim 13$, and then gradually decreases below $z \sim 10$. The Pop III star formation remains roughly constant for more than 400 Myr. The Pop III star formation of the *Normal* region also appears to plateau at $z \sim 13$, albeit at a higher rate than the *Void* region. As discussed in [Xu et al. \(2013, 2016a\)](#) the Pop III formation is regulated through suppression of their formation in low mass halos by the Lyman-Werner radiation from stellar feedback. However their formation is not suppressed in halos of mass $\sim 10^7 M_\odot$ and above, despite strong photodissociating radiation. The plateaus reflect the rates at which pristine halos of

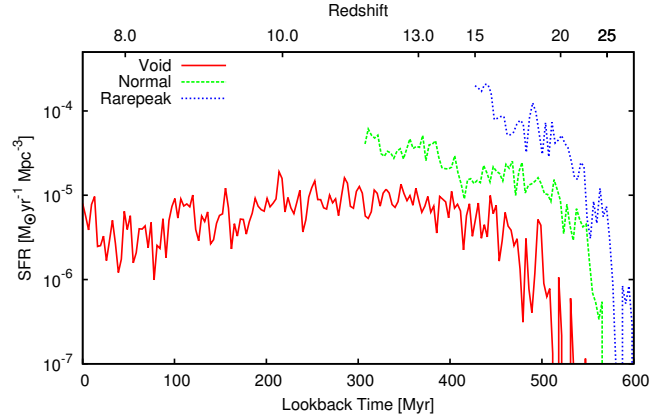


Figure 1. Evolution of Pop III star formation rate densities of *Rarepeak*, *Normal* and *Void* regions.

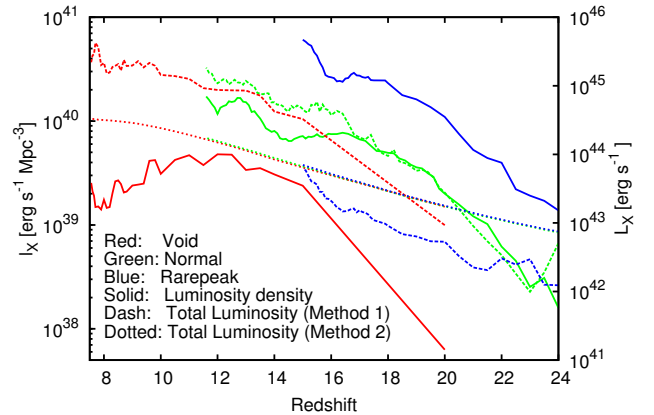


Figure 2. Evolution of X-ray luminosity density in the refined regions (solid lines) and total X-ray luminosity of the entire $(40 \text{ Mpc})^3$ simulation volume (dashed and dotted lines). Dashed lines show the total luminosity extrapolated from *Rarepeak*, *Normal*, and *Void* regions, respectively, using Method 1. Dotted lines show the total X-ray luminosity obtained from Method 2. Since this method uses a single correlation function between X-ray emission and gas density and redshift, using the data from all three simulations together, the total X-ray luminosities predicted for the three runs are almost the same.

sufficient mass are forming in these different environments.

Figure 2 shows the evolution of the X-ray luminosity densities of the refined regions and the total X-ray luminosities of the whole box. The X-ray luminosity densities simply follow the Pop III star formation rate densities. Consequently, at $z = 15$, the cosmic variance effect on the predicted X-ray emissivity density is about an order of magnitude. Using Method 1, the total X-ray luminosities are underestimated for the *Rarepeak*, and overestimated for the *Void* run. To better estimate the X-ray background, we scale down the total luminosity from the *Void* region to match that from the *Normal* simulation. Using Method 2, we obtain a very smooth X-ray luminosity evolution. It grows from 1.7×10^{43} to $3 \times 10^{44} \text{ erg s}^{-1}$ from $z = 20$ to $z = 7.6$, as the luminosity density grows from 2.7×10^{38} to $4.7 \times 10^{39} \text{ erg s}^{-1} \text{ Mpc}^{-3}$. This is a factor of $30(\epsilon_{\text{bin}}/0.5)$ higher than estimates of the X-ray luminosities from normal X-ray binaries and AGN ([Fragos et al. 2013](#); [Madau & Fragos 2016](#)). Taking the result from Method 2 as our reference, we would conclude that Method 1 is accurate to $\pm 50\%$ at the redshifts where they overlap.

Mean background X-ray intensities are shown in Figure 3.

² <http://yt-project.org>

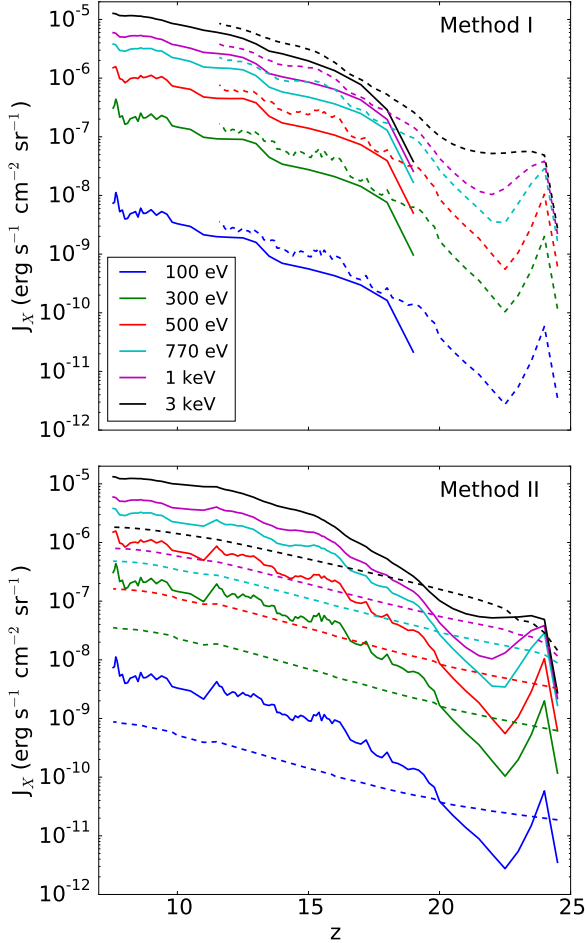


Figure 3. Evolution of the mean X-ray background intensities for different observed X-ray energies. Upper panel: results from *Void* (solid line) and *Normal* (dashed line) simulations using Method 1. Lower panel: same as upper panel but using Method 2. The background intensity is the summation of all the redshifted radiation observed.

We assume the X-ray sources are monochromatic and calculate the background for six different photon energies. The X-ray intensity at an observer redshift is the total intensity of observed redshifted X-rays from all earlier redshifts. In the upper panel, we show the X-ray background intensities from *Void* and *Normal* simulations using X-ray emissions calculated using Method 1. In the lower panel, we do the same thing using Method 2. In both cases the X-ray background gradually builds up, and is significantly dependent on the emitted photon energy. As discussed in Xu et al. (2014), only the high energy (keV) photons accumulate to form a global background since sub-keV photons are absorbed near the source. The X-ray background intensity of 3 keV photons from Method 2, which we consider more reliable than Method 1, is over $10^{-6} \text{ erg s}^{-1} \text{ cm}^{-2} \text{ sr}^{-1}$.

Figure 4 illustrates the X-ray background spectra for different source photon energies for different models at $z = 12$ and $z = 7.6$ showing how X-ray photons with different energies from higher redshifts contribute to the X-ray background. Figure 5 shows the synthetic X-ray spectra at $z = 12$ and $z = 7.6$ by assuming the source X-ray energies are equally distributed over the six energy bands. The high energy keV photons with low absorption produce continuous broad band observed spectra by cosmological redshifting. Except for the gap between 1 and 1.5 keV for the $z = 12$ spectrum due to the red-

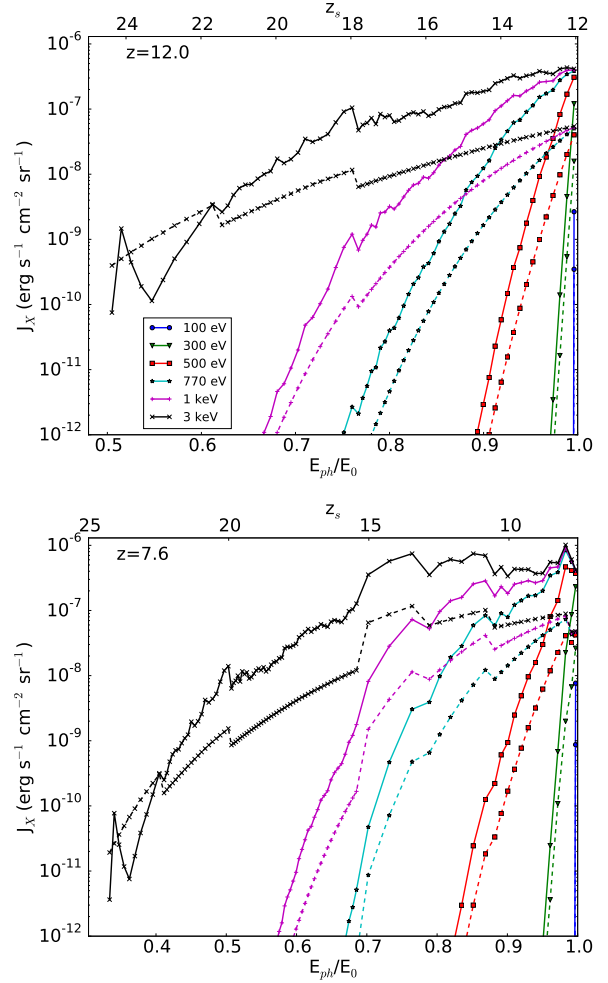


Figure 4. Mean X-ray background spectra at redshifts $z = 12$ and $z = 7.6$ for different monochromatic X-ray source energies. Solid lines are for Method 1, and dashed lines are Method 2. The lower x-axis is the ratio of observed photon energy to source photon energy, while the upper x-axis is the source redshift.

shift cutoff, the X-ray spectra have similar strengths at $z = 12$ and $z = 7.6$, as the Pop III star formation rate does not evolve much. At $z = 7.6$, keV X-rays from early times redshift to sub-keV energies and then heat and ionize the IGM. Using a one-zone calculation Xu et al. (2014) showed that the X-rays of 1 keV and 3 keV in this spectrum have similar heating and ionizing effects to the IGM. The efficient absorption of X-rays happens below ~ 500 -600 eV, and any X-rays with photon energies lower than this are absorbed locally and only contribute a narrow band to the spectrum.

4. SUMMARY AND DISCUSSION

In this Letter, we present estimates of the X-ray emission and background from Pop III binaries derived from the Pop III star formation histories in *Renaissance Simulations* beginning at $z \sim 25$ down to $z = 7.6$ near the end of reionization. The key results are summarized as follows:

1. A significant amount of X-rays may be produced by Pop III binaries down to the end of reionization, as a direct result of Pop III stars forming continuously with steady rates since they begin forming at redshifts of 20–30.
2. The X-ray background builds up gradually once the first

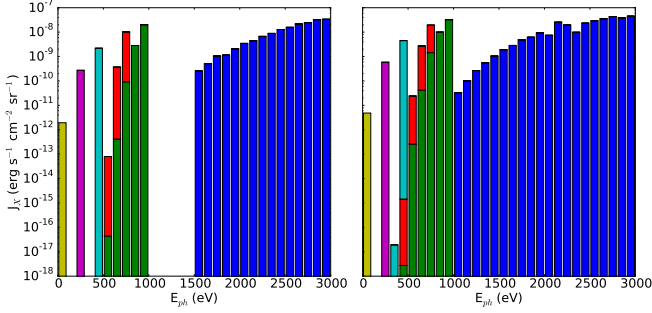


Figure 5. Synthetic X-ray spectra at $z = 12$ (left) and $z = 7.6$ (right) from Method 2 by assuming source X-rays are equally distributed over all six energy bands. X-axis is the observed photon energy. X-ray intensities of different energy sources are in different colors with the same scheme as Figure 4 and are stacked.

stars begin forming. The X-ray background intensity depends on the assumed source photon energies. Only keV photons contribute to the X-ray background, and become a broad band spectrum in the background.

3. X-rays from Pop III binaries might continuously dominate X-rays from normal stellar X-ray binaries and AGN until the end of reionization, although this conclusion depends on the assumed fraction of Pop III stars that become X-ray binaries.

The results of this *Letter* may have important implications on the understanding of the reionization process, the properties of the post-reionization IGM, and many cosmological observations, like the Thomson scattering optical depth of the cosmic microwave background, neutral hydrogen 21-cm transition line, and the Ly α forest.

The Pop III binary X-ray luminosity per unit comoving volume is estimated to be $\log I_X \simeq (\epsilon_{\text{bin}}/0.5)[40.87 - 0.12(1+z)]$ in units of $\text{erg s}^{-1} \text{Mpc}^{-3}$, which is likely higher than those from other X-ray sources of AGNs and normal XRBs at redshifts higher than 6 (Fragos et al. 2013). This linear fit is only valid at $z \geq 10$ and has a maximum error of 0.5% compared to the computed values. This is based on our assumption at 50% of all Pop III stars form in binaries, and evolve through a high mass XRB phase. Since it takes a long time for the X-ray background to build up, the contribution from Pop III binaries may continue to dominate the X-ray background down to much lower redshifts.

Recently Fialkov et al. (2016) used the unresolved soft X-ray background to place constraints on the nature of high redshift X-ray sources. They derived constraints on the X-ray efficiency parameter f_x for three source types and two reionization scenarios, where f_x is defined implicitly by the relation (Furlanetto et al. 2006; Fragos et al. 2013)

$$\frac{L_X}{SFR} = 3 \times 10^{40} f_x \text{ erg s}^{-1} \text{M}_{\odot}^{-1} \text{yr}, \quad (1)$$

where here SFR refers to the normal (Pop II) star formation rate density. Using the Method 2 value of $L_X \approx 5 \times 10^{39} \text{ erg s}^{-1} \text{Mpc}^{-3}$ at $z = 7.6$, and the observed SFR of $10^{-2} \text{M}_{\odot} \text{yr}^{-1} \text{Mpc}^{-3}$ (Bouwens et al. 2015), we get $f_x \approx 16$, well within observational constraints for all cases considered.

It is interesting to compare the relative importance of ionizing UV and X-ray photons during the course of the simulations. To $z = 7.6$, both Pop III and metal-enriched stars produce about 1.4×10^{71} erg in ionizing UV photons (or about

6.3×10^{69} photons) inside the refined region, of which less than 1% (10^{69} erg), is produced by Pop III stars. There are about 7.6×10^{68} hydrogen atoms in the survey volume of the *Void* run. At $z = 7.6$, only $\sim 13.2\%$ hydrogen atoms have been ionized by the UV ionizing photons in the simulation (Xu et al. 2016b). So most of the ionizing UV photons are absorbed by hydrogen atoms that later recombine and are consumed to maintain the ionization state of high density regions. On the contrary, a large fraction of X-rays are expected to penetrate to low density regions which have recombination times longer than the Hubble time. During the same period, the Pop III binaries of the *Void* simulation produced $\sim 6.8 \times 10^{69}$ eV of energy in X-rays inside the refined region. It is about 5% of energy of ionizing UV photons and about 9 eV per hydrogen atom. Using Method 2, we estimate that Pop III binaries produce in total 2.1×10^{72} eV of energy in X-rays in the entire simulation box. As there are about 3.6×10^{71} hydrogen atoms in the simulation box, this amounts to about 6 eV of X-ray energy per hydrogen atom.

This photon budget analysis shows that the X-ray component is not negligible. There is enough energy in X-rays from Pop III binaries to significantly change the thermal and ionization states of the IGM. It is very hard to know the ratio of X-ray energy used in ionizing and heating the IGM without knowing the SED of the X-ray sources and doing a detailed simulation (Shull & van Steenberg 1985). Xu et al. (2014) used a one-zone model to calculate heating and ionizing effects for fixed X-ray photon energies and fluxes and to estimate the temperature and hydrogen ionization fraction of the *Rarepeak* simulation volume by simply assuming the X-ray background is constant since $z = 15$. This predicted that the IGM may be heated to several hundred Kelvin and be ionized to about 0.5% by $z = 6$. We have shown that the X-ray luminosity and background actually increase until the end of the simulation at $z = 7.6$ and are at much higher (~ 10 times) levels. The electron fraction due to X-ray ionization might therefore reach a few percent by simply extrapolating the results in Xu et al. (2014), or even more since X-rays are also efficient at helium ionization. This physics is important to the understanding the optical depth of CMB. In addition, by the end of reionization, the IGM may have been homogeneously heated by the keV photons of the X-ray background for hundreds of Myr. The additional heat input above and beyond the UV photoheating may reach thousands of Kelvin (Xu et al. 2014), and that is enough to have important impacts on high redshift 21-cm signatures (Ahn et al. 2015) and the Ly α forest spectra (Tytler et al. 2009) at lower redshifts.

This research is part of the Blue Waters project, which a joint effort supported by the NSF (award number ACI-1238993) and the state of Illinois, using NSF PRAC OCI-0832662. This research was supported by NSF grants PHY-0941373, AST-1109243, AST-1211626, and AST-1333360, and NASA grants NNX12AC98G, NNX15AP39G, HST-AR-13261.01-A, HST-AR-13895.001, HST-AR-14315.001-A, HST-AR-14326.001. K.A. was supported by NRF-2012K1A3A7A03049606 and NRF-2014R1A1A2059811. This work was performed using the open-source ENZO and YT codes, which are the products of collaborative efforts of many independent scientists from institutions around the world. Their commitment to open science has helped make

this work possible.

REFERENCES

- Abel, T., Anninos, P., Zhang, Y., & Norman, M. L. 1997, *New Astronomy*, 2, 181
- Abel, T., Bryan, G. L., & Norman, M. L. 2002, *Science*, 295, 93
- Ahn, K., Iliev, I. T., Shapiro, P. R., Mellema, G., Koda, J., & Mao, Y. 2012, *ApJL*, 756, L16
- Ahn, K., Shapiro, P. R., Iliev, I. T., Mellema, G., & Pen, U.-L. 2009, *ApJ*, 695, 1430
- Ahn, K., Xu, H., Norman, M. L., Alvarez, M. A., & Wise, J. H. 2015, *ApJ*, 802, 8
- Alvarez, M. A., Wise, J. H., & Abel, T. 2009, *ApJL*, 701, L133
- Barkana, R., & Loeb, A. 2004, *ApJ*, 609, 474
- Bouwens, R. J., et al. 2015, *ApJ*, 803, 34
- Bromm, V., Coppi, P. S., & Larson, R. B. 2002, *ApJ*, 564, 23
- Bromm, V., Ferrara, A., Coppi, P. S., & Larson, R. B. 2001, *MNRAS*, 328, 969
- Bryan, G. L., et al. 2014, *ApJS*, 211, 19
- Chen, P., Wise, J. H., Norman, M. L., Xu, H., & O’Shea, B. W. 2014, *ApJ*, 795, 144
- Clark, P. C., Glover, S. C. O., & Klessen, R. S. 2008, *ApJ*, 672, 757
- Fan, X., Carilli, C. L., & Keating, B. 2006, *ARA&A*, 44, 415
- Fialkov, A., & Barkana, R. 2014, *MNRAS*, 445, 213
- Fialkov, A., Barkana, R., & Visbal, E. 2014, *Nature*, 506, 197
- Fialkov, A., Barkana, R., Visbal, E., Tseliakhovich, D., & Hirata, C. M. 2013, *MNRAS*, 432, 2909
- Fialkov, A., Cohen, A., Barkana, R., & Silk, J. 2016, *ArXiv e-prints*
- Fragos, T., Lehmer, B. D., Naoz, S., Zezas, A., & Basu-Zych, A. 2013, *ApJL*, 776, L31
- Furlanetto, S. R., Oh, S. P., & Briggs, F. H. 2006, *Physics Reports*, 433, 181
- Greif, T. H., Bromm, V., Clark, P. C., Glover, S. C. O., Smith, R. J., Klessen, R. S., Yoshida, N., & Springel, V. 2012, *MNRAS*, 424, 399
- Greif, T. H., White, S. D. M., Klessen, R. S., & Springel, V. 2011, *ApJ*, 736, 147
- Hahn, O., & Abel, T. 2011, *MNRAS*, 415, 2101
- Haiman, Z. 2011, *Nature*, 472, 47
- Heger, A., Fryer, C. L., Woosley, S. E., Langer, N., & Hartmann, D. H. 2003, *ApJ*, 591, 288
- Hirano, S., Hosokawa, T., Yoshida, N., Omukai, K., & Yorke, H. W. 2015, *MNRAS*, 448, 568
- Hosokawa, T., Hirano, S., Kuiper, R., Yorke, H. W., Omukai, K., & Yoshida, N. 2016, *ApJ*, 824, 119
- Komatsu, E., et al. 2011, *ApJS*, 192, 18
- Kuhlen, M., & Madau, P. 2005, *MNRAS*, 363, 1069
- Madau, P., & Fragos, T. 2016, *ArXiv e-prints* (1606.07887)
- Mesinger, A., Ferrara, A., & Spiegel, D. S. 2013, *MNRAS*, 431, 621
- Mirabel, I. F., Dijkstra, M., Laurent, P., Loeb, A., & Pritchard, J. R. 2011, *A&A*, 528, A149
- Mirocha, J., Furlanetto, S. R., & Sun, G. 2016, *ArXiv e-prints*
- Oh, S. P. 2001, *ApJ*, 553, 499
- Omukai, K., Tsuribe, T., Schneider, R., & Ferrara, A. 2005, *ApJ*, 626, 627
- O’Shea, B. W., & Norman, M. L. 2007, *ApJ*, 654, 66
- O’Shea, B. W., Wise, J. H., Xu, H., & Norman, M. L. 2015, *ApJL*, 807, L12
- Ostriker, J. P., & Gnedin, N. Y. 1996, *ApJL*, 472, L63
- Pacucci, F., Mesinger, A., Mineo, S., & Ferrara, A. 2014, *MNRAS*, 443, 678
- Pritchard, J. R., & Furlanetto, S. R. 2007, *MNRAS*, 376, 1680
- Pritchard, J. R., & Loeb, A. 2012, *Reports on Progress in Physics*, 75, 086901
- Ricotti, M., & Ostriker, J. P. 2004, *MNRAS*, 352, 547
- Ricotti, M., Ostriker, J. P., & Gnedin, N. Y. 2005, *MNRAS*, 357, 207
- Schaerer, D. 2002, *A&A*, 382, 28
- Schneider, R., Omukai, K., Inoue, A. K., & Ferrara, A. 2006, *MNRAS*, 369, 1437
- Shull, J. M., & van Steenberg, M. E. 1985, *ApJ*, 298, 268
- Smith, B. D., Turk, M. J., Sigurdsson, S., O’Shea, B. W., & Norman, M. L. 2009, *ApJ*, 691, 441
- Stacy, A., Bromm, V., & Loeb, A. 2011, *ApJL*, 730, L1
- Stacy, A., Greif, T. H., & Bromm, V. 2010, *MNRAS*, 403, 45
- Susa, H., Hasegawa, K., & Tominaga, N. 2014, *ApJ*, 792, 32
- Tanaka, T., Perna, R., & Haiman, Z. 2012, *MNRAS*, 425, 2974
- Turk, M. J., Abel, T., & O’Shea, B. 2009, *Science*, 325, 601
- Turk, M. J., Smith, B. D., Oishi, J. S., Skory, S., Skillman, S. W., Abel, T., & Norman, M. L. 2011, *ApJS*, 192, 9
- Tytler, D., Paschos, P., Kirkman, D., Norman, M. L., & Jena, T. 2009, *MNRAS*, 393, 723
- Venkatesan, A., Giroux, M. L., & Shull, J. M. 2001, *ApJ*, 563, 1
- Visbal, E., Barkana, R., Fialkov, A., Tseliakhovich, D., & Hirata, C. M. 2012, *Nature*, 487, 70
- Wise, J. H., & Abel, T. 2008, *ApJ*, 684, 1
- . 2011, *MNRAS*, 414, 3458
- Wise, J. H., Abel, T., Turk, M. J., Norman, M. L., & Smith, B. D. 2012a, *MNRAS*, 427, 311
- Wise, J. H., Demchenko, V. G., Halicek, M. T., Norman, M. L., Turk, M. J., Abel, T., & Smith, B. D. 2014, *MNRAS*, 442, 2560
- Wise, J. H., Turk, M. J., Norman, M. L., & Abel, T. 2012b, *ApJ*, 745, 50
- Xu, H., Ahn, K., Wise, J. H., Norman, M. L., & O’Shea, B. W. 2014, *ApJ*, 791, 110
- Xu, H., Norman, M. L., O’Shea, B. W., & Wise, J. H. 2016a, *ApJ*, 823, 140
- Xu, H., O’Shea, B. W., Collins, D. C., Norman, M. L., Li, H., & Li, S. 2008, *ApJL*, 688, L57
- Xu, H., Wise, J. H., & Norman, M. L. 2013, *ApJ*, 773, 83
- Xu, H., Wise, J. H., Norman, M. L., Ahn, K., & O’Shea, B. W. 2016b, *ArXiv e-prints* (1604.07842)